JOURNAL OF GEOPHYSICAL RESEARCH, VOL. 102, NO. C5, PAGES 10,457–10,471, MAY 15, 1997

Global oceanic precipitation: A joint view by TOPEX and the TOPEX microwave radiometer

Ge Chen[1]
Ocean Remote Sensing Institute, Ocean University of Qingdao, Qingdao, China

Bertrand Chapron, Jean Tournadre, and Kristina Katsaros
Département d'Océanographie Spatiale, Centre de Brest, IFREMER, Plouzané, France

Douglas Vandemark
Wallops Flight Facility, NASA Goddard Space Flight Center, Wallops Island, Virginia

Abstract. The TOPEX/POSEIDON mission offers the first opportunity to observe rain cells over the ocean by a dual-frequency radar altimeter (TOPEX) and simultaneously observe their natural radiative properties by a three-frequency radiometer (TOPEX microwave radiometer (TMR)). This work is a feasibility study aimed at understanding the capability and potential of the active/passive TOPEX/TMR system for oceanic rainfall detection. On the basis of past experiences in rain flagging, a joint TOPEX/TMR rain probability index is proposed. This index integrates several advantages of the two sensors and provides a more reliable rain estimate than the radiometer alone. One year's TOPEX/TMR data are used to test the performance of the index. The resulting rain frequency statistics show quantitative agreement with those obtained from the Comprehensive Ocean-Atmosphere Data Set (COADS) in the Intertropical Convergence Zone (ITCZ), while qualitative agreement is found for other regions of the world ocean. A recent finding that the latitudinal frequency of precipitation over the Southern Ocean increases steadily toward the Antarctic continent is confirmed by our result. Annual and seasonal precipitation maps are derived from the index. Notable features revealed include an overall similarity in rainfall pattern from the Pacific, the Atlantic, and the Indian Oceans and a general phase reversal between the two hemispheres, as well as a number of regional anomalies in terms of rain intensity. Comparisons with simultaneous Global Precipitation Climatology Project (GPCP) multisatellite precipitation rate and COADS rain climatology suggest that systematic differences also exist. One example is that the maximum rainfall in the ITCZ of the Indian Ocean appears to be more intensive and concentrated in our result compared to that of the GPCP. Another example is that the annual precipitation produced by TOPEX/TMR is constantly higher than those from GPCP and COADS in the extratropical regions of the northern hemisphere, especially in the northwest Pacific Ocean. Analyses of the seasonal variations of prominent rainy and dry zones in the tropics and subtropics show various behaviors such as systematic migration, expansion and contraction, merging and breakup, and pure intensity variations. The seasonality of regional features is largely influenced by local atmospheric events such as monsoon, storm, or snow activities. The results of this study suggest that TOPEX and its follow-on may serve as a complementary sensor to the special sensor microwave/imager in observing global oceanic precipitation.

1. Introduction

Global oceanic precipitation is one of the most needed but least known geophysical parameters. Oceanic rainfall plays a key role in defining regional and global climate, being responsible for most of the freshwater flux to the sea and serving as a link in the global hydrological and geochemical cycles. The associated latent heat release is of great importance for the general circulation of the atmosphere. Further progress in understanding the El Niño–Southern Oscillation (ENSO) could also be made with more reliable data on tropical rainfall. However, continuous and accurate measurement of rain over the global ocean is extremely difficult, owing to its intermittent nature and highly variable intensity, as well as the well-known limitations of the conventional ship observations.

In view of its geophysical importance and the observational difficulties, tremendous efforts have been expended in the past 2 decades to extract rain signatures and to derive rain parameters from spaceborne sensors ranging from visible and infrared radiometers (e.g., GOES [*Barrett and Martin*, 1981; *Janowiak and Arkin*, 1991], Meteosat [*Cheng and Brown*, 1995]), passive microwave radiometers (e.g., scanning multichannel

[1]Also at Département d'Océanographie Spatiale, Centre de Brest, IFREMER, Plouzané, France.

Paper number 97JC00047.
0148-0227/97/97JC-00047$09.00

microwave radiometer (SMMR)/Nimbus 7 [*Petty and Katsaros*, 1992], microwave sounding unit (MSU)/NOAA [*Spencer*, 1993], special sensor microwave/imager (SSM/I) [*Wilheit et al.*, 1994]), microwave scatterometer (e.g., SASS/Seasat [*Black et al.*, 1985]), radar altimeter (e.g., ERS 1 [*Guymer et al.*, 1995], TOPEX/POSEIDON [*Quartly et al.*, 1996; *Tournadre and Morland*, 1997]), to synthetic aperture radar (e.g., Seasat [*Atlas*, 1994]). Among the various satellite sensors mentioned above, the SSM/I, beginning in 1987, has so far been considered as the most successful one in measuring oceanic precipitation. It is widely accepted that the SSM/I radiometers have introduced a new era of data continuity and quality which alleviates the severe shortage of reliable in situ precipitation observations over much of the world ocean. Although the value of SSM/I rainfall measurements is beyond doubt, it should nevertheless be noted that much of the confidence on its performance is based on the well-established physical background (scattering and radiation); the same lack of in situ data has ultimately hampered a direct and independent evaluation. A recent intercomparison of oceanic precipitation frequencies from 10 SSM/I rain rate algorithms and shipboard present weather reports shows that although most algorithms yield distributions in reasonable agreement with ship-derived climatology at low latitudes, the majority fail to register more than very infrequent (around 1%) precipitation at latitudes poleward of about 45°, in contrast to the much larger (around 10%) frequencies indicated by surface reports [*Petty*, 1997]. Moreover, all 10 algorithms appear to have difficulties in producing realistic precipitation frequencies in the "dry" subtropical trade wind belts where physical characteristics are thought to be unique. These results reveal some of the weaknesses of the sensor and suggest that new methods stemming from different physical principles are highly desirable for satellite observation of oceanic precipitation.

A number of previous studies have demonstrated that a satellite altimeter is a useful sensor for rain detection. Works in this field were initially stimulated by the need of flagging rain-contaminated measurements so as to obtain accurate and unbiased altimeter data. The first observation of rain affecting spaceborne altimeter measurements appears to have been reported in the Seasat Gulf of Alaska Workshop [*Jet Propulsion Laboratory, California Institute of Technology*, 1979, Figures 5–16], which described a possible rain cell encounter, resulting in anomalies in the measured backscatter coefficient, sea surface height, and significant wave height. A subsequent attempt was made for a more systematic study of rain effects on Seasat altimeter data [*Srokosz and Guymer*, 1988]. Three cases which spanned a range of conditions in terms of extent and intensity of rain were examined. The main conclusion drawn from the limited Seasat study was that the most obvious effect of rain on altimeter data was on the backscatter coefficient, σ^0. Therefore changes in σ^0 seem to be a possible method of detecting rain with the altimeter. To check and extend these conclusions, a more comprehensive study is performed with ERS 1, which also carries a Ku band altimeter like Seasat [*Guymer et al.*, 1995]. *Guymer et al.*'s [1995] results confirm that all rain events are associated with a sharp drop in the value of σ^0 and an increase in its variability. However, an accompanying enhanced backscatter can also occur, possibly as a result of short wave damping by rain. In addition, high rain rate can distort the return waveforms, leading to erroneous measurements of sea surface height and significant wave height. They argue that improved rain flags for ERS altimeters may come from the joint use of several effective thresholds, such as 2 dB for backscatter change within eight successive measurements, 0.25 m for the standard deviation of sea surface height, and 0.1 dB for liquid water content correction derived from the along-track scanning radiometer/microwave sounder (ATSR/M). The TOPEX altimeter provides a new opportunity for detecting oceanic rainfall, thanks to its dual-frequency (C and Ku band) capacity. In a recent study by *Tournadre and Morland* [1997] using two cycles of TOPEX data (cycles 3 and 8), a new rain flag based on a departure from the normal relationship between Ku and C band backscatter is proposed; that is, measurements with a difference between the expected and observed σ^0_{Ku} exceeding 1.9 times of the corresponding standard deviation, in conjunction with the TMR-derived liquid water content greater than 200 μm, are identified as rain events. This flag is found to be able to signal all the 64 probable rain events in the North Atlantic identified by visual inspection. In a parallel study by *Quartly et al.* [1996] using 80 days of TOPEX data, a similar approach based on rain-induced Ku/C attenuation discrepancy is adopted. The only difference is that they use a fixed threshold of 0.5 dB instead of a varying standard deviation. The results of the overlapping parts of the two studies are in agreement. In addition, *Tournadre and Morland* [1997] propose an estimation of the rainfall rate from the attenuation of the Ku band backscatter, while *Quartly et al.* [1996] provide a preliminary discussion on the geographical and seasonal changes of rain-contaminated altimeter data.

The general approach of existing altimetric rain detection studies consists of three steps: (1) visual inspection of rain-affected parameters and subjective decision of rain events, (2) rain criteria definitions and tests, and (3) seeking independent support from other satellite data or synoptic weather charts. Unfortunately, none of the reported rain effects on altimeters have been directly confirmed by in situ observations. Given the difficulties in obtaining surface rain measurements over the ocean, direct validation seems to be unlikely in the foreseeable future. However, on the basis of past experiences with the Seasat, ERS, and TOPEX altimeters, we believe that it is now possible to conduct a more convincing verification of altimeter rain estimates. One way to do so is to make statistical comparisons with existing rain climatology on global and seasonal scales. This forms the principal motivation of the present study. A further motivation comes from the hope that the unprecedented dual-frequency capability of the TOPEX altimeter may also bring new information on global oceanic precipitation. A final motivation is that the simultaneous flight of a dual-frequency altimeter and a three-frequency radiometer on TOPEX offers an opportunity for intercomparison of the strengths and weaknesses of each type of sensor for rain detection, in the hope that an improved rain estimate can be achieved through an optimal combination of data from the two sensors.

The idea of this study is to define a rain index which integrates the TOPEX and TOPEX microwave radiometer (TMR) measurements and which is comparable to conventional rain climatology. It is noted that a commonly adopted approach in altimetric rain detection is setting thresholds on some measured or derived geophysical parameters [*Guymer et al.*, 1995; *Quartly et al.*, 1996; *Tournadre and Morland*, 1997]. For our purpose we combine and modify various thresholds and extend them to generate a normalized rain probability index (section 2). We then produce global and seasonal statistics of the proposed index using 1 year of TOPEX data (see Table 1 for a

Table 1. Summary of TOPEX Data Used in This Study

Cycle Number	Starting Date	Ending Date	Number of Valid Data	Remarks*
8	Dec. 1, 1992	Dec. 11, 1992	164,976	
9	Dec. 11, 1992	Dec. 21, 1992	384,457	
10	Dec. 21, 1992	Dec. 31, 1992	483,152	
11	Dec. 31, 1992	Jan. 10, 1993	433,961	passes 219–245 P on
12	Jan. 10, 1993	Jan. 20, 1993	386,447	passes 21–46, 217–243 P on
13	Jan. 20, 1993	Jan. 30, 1993	427,996	passes 219–254 P on
14	Jan. 30, 1993	Feb. 8, 1993	414,228	passes 1–45 P on
15	Feb. 8, 1993	Feb. 18, 1993	435,282	passes 217–247 P on
16	Feb. 18, 1993	Feb. 28, 1993	390,380	passes 2–47 P on
17	Feb. 28, 1993	March 10, 1993	502,019	
18	March 10, 1993	March 20, 1993	499,754	
19	March 20, 1993	March 30, 1993	492,661	
20	March 30, 1993	April 9, 1993	0	passes 1–254 P on
21	April 9, 1993	April 19, 1993	492,422	
22	April 19, 1993	April 29, 1993	492,800	
23	April 29, 1993	May 9, 1993	487,513	
24	May 9, 1993	May 19, 1993	442,926	data error for passes 101–122
25	May 19, 1993	May 29, 1993	479,166	
26	May 29, 1993	June 7, 1993	474,901	
27	June 7, 1993	June 17, 1993	470,114	
28	June 17, 1993	June 27, 1993	467,351	
29	June 27, 1993	July 7, 1993	463,276	
30	July 7, 1993	July 17, 1993	458,278	
31	July 17, 1993	July 27, 1993	0	passes 1–254 P on
32	July 27, 1993	Aug. 6, 1993	453,946	
33	Aug. 6, 1993	Aug. 16, 1993	425,704	
34	Aug. 16, 1993	Aug. 26, 1993	451,691	
35	Aug. 26, 1993	Sept. 5, 1993	451,370	
36	Sept. 5, 1993	Sept. 15, 1993	452,085	
37	Sept. 15, 1993	Sept. 25, 1993	407,682	
38	Sept. 25, 1993	Oct. 4, 1993	456,326	
39	Oct. 4, 1993	Oct. 14, 1993	455,579	
40	Oct. 14, 1993	Oct. 24, 1993	456,057	
41	Oct. 24, 1993	Nov. 3, 1993	0	passes 1–254 P on
42	Nov. 3, 1993	Nov. 13, 1993	458,505	
43	Nov. 13, 1993	Nov. 23, 1993	458,875	
44	Nov. 23, 1993	Dec. 3, 1993	448,154	

*P denotes Poseidon.

summary) and make comparisons with the Global Precipitation Climatology Project (GPCP) [*Huffman et al.*, 1997] and Comprehensive Ocean-Atmosphere Data Set (COADS) [*Woodruff et al.*, 1987; *da Silva et al.*, 1994] oceanic rain climatologies (sections 3 and 4). In particular, we take advantage of significant recent progress in surface rain analysis, such as the work by *Petty* [1995] which provides a solid basis for evaluating the ability of satellite techniques to estimate fractional coverage by precipitation over oceanic areas. As will be stressed in the summary (section 5), the TOPEX/TMR rain estimates compare well with similar results based on GPCP and COADS data. Therefore altimetric observation may represent a new method of oceanic rain detection from space.

2. Definition of Rain Probability Index

It is well known that multifrequency techniques are advantageous in satellite ocean remote sensing. This heritage is also used to explore the possibility of altimetric rain detection. *Goldhirsh and Walsh* [1982] are among the first who try to apply this idea to TOPEX. The feasibility of such a consideration is largely based on the work of *Olsen et al.* [1978], who show that rain attenuation at Ku band is greater than that at C band by an order of magnitude under a wide range of rain rates. After the TOPEX data became available, a practical scheme based on the differential effect of rain on Ku and C band measurements is worked out by *Tournadre and Morland* [1997] as an attempt to define a new rain flag for TOPEX. The rain probability index which will be introduced below is an extension of that scheme.

2.1. Determination of a Normal Ku/C Band Relationship For σ^0

Following a data screening which eliminates points (1) over land or ice, (2) with problems in measurement conditions, and (3) with off-nadir angle greater than 0.2° [see *Archiving, Validation, and Interpretation of Satellite Data in Oceanography* (*AVISO*), 1992], the normal relationships of the Ku/C σ^0 and their associated standard deviations for TOPEX cycles 8–44 (excluding cycles 20, 31, and 41 for which the POSEIDON altimeter is on; see Table 1) which span December 1992 and November 1993 are plotted in Figure 1. Each of the curves in Figure 1a is obtained by iterative calculation of the mean value of σ^0_C at a given σ^0_{Ku} and so is the standard deviation (Figure 1b). In the second computation, points lying beyond 3 standard deviations from the first mean are removed in order to eliminate outliers. Figure 1 shows that within the band of 8 dB $< \sigma^0_{Ku} <$ 16 dB, where the majority of measurements lie, both the mean values and the standard deviations are highly convergent. It implies that criteria based on this relationship will be

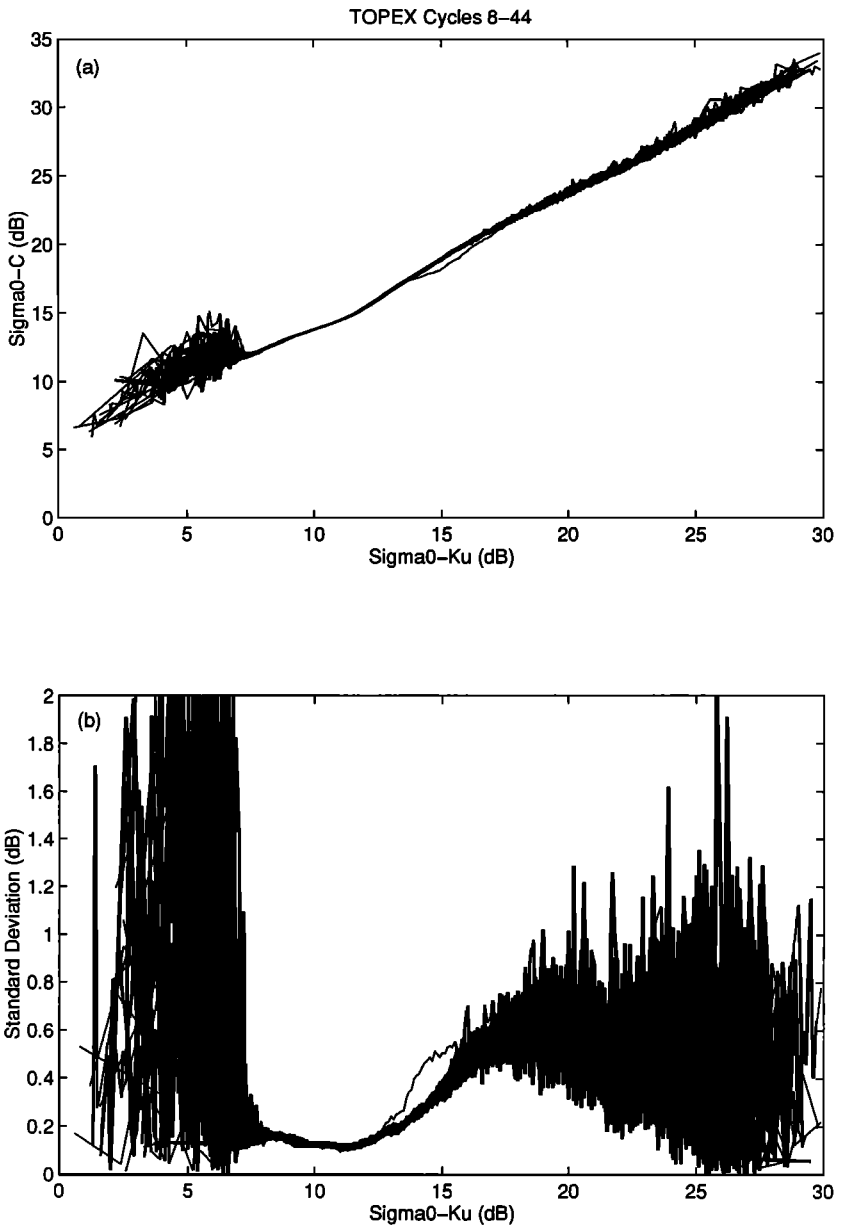

Figure 1. (a) The mean relationships between σ^0_{Ku} and σ^0_C for TOPEX cycles 8–44. (b) The corresponding standard deviations of σ^0_C with respect to σ^0_{Ku}.

consistent from cycle to cycle without calibration. Beyond this band, considerable spread in the mean values and dramatic scatter in the standard deviations are evident. This is mainly due to the decreasing number of measurements associated with extreme wind fields. In addition, two unusual features are worth mentioning. First, a significant kink is observed in the normal Ku/C relation at $\sigma^0_{Ku} = 12$ dB (Figure 1a), which coincides with a minimum (about 0.1 dB) in the standard deviation (Figure 1b). This results from the fact that the kink corresponds to the largest number of samples per decibel and indicates the statistical significance of the analysis. Second, the only cycle whose Ku/C relationship differs considerably from others is cycle 24, which covers May 9–19, 1993. In this cycle the σ^0_C appears to be 1–2 dB lower than normal values around 13 dB $< \sigma^0_{Ku} <$ 17 dB (Figure 1a), and the standard deviation shows a corresponding increase (Figure 1b). This anomaly was eventually traced back to an error in the preprocessing of the instrument files for passes 101–122 and therefore does not undermine our analysis scheme.

2.2. Definition of a Joint TOPEX/TMR Rain Probability Index

The idea of defining a joint TOPEX/TMR rain probability index has several expected advantages. First, from the sensor point of view, information from five microwave frequencies (5.3, 13.6, 18.0, 21.0, and 37.0 GHz) will be integrated, leading to a complementary sensing of the rain effects. Second, taking into account the complex and sporadic nature of the rain, probability is certainly a more appropriate term than any threshold-based categorical classification. Third, from a statistical point of view the introduction of a probability index will allow nearly 10% of the valid data, rather than otherwise around 1% of certain rain cases only, to be used in a quanti-

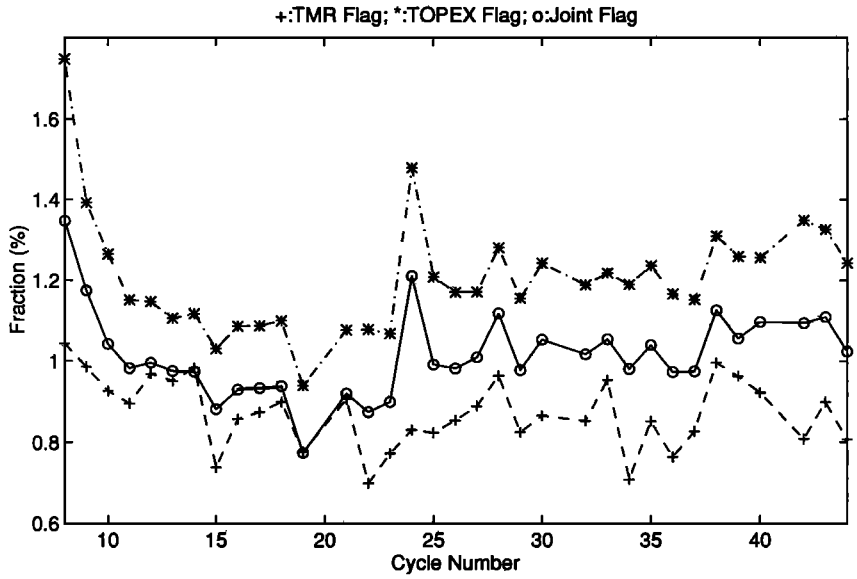

Figure 2. Fraction of measurements with $P_A = 1$ (stars), $P_R = 1$ (pluses), and $P_J = 1$ (circles) for TOPEX cycles 8–44.

tative way (see next section). This is thought to greatly increase the statistical significance of the resultant rain estimates.

In order to examine the contribution and effectiveness of each sensor for rain detection, we first define two separate probability indexes, P_A and P_R, corresponding to the TOPEX altimeter and the TMR radiometer, respectively,

$$P_A = \frac{\sigma_C^0 - f(\sigma_{Ku}^0)}{N_1 s(\sigma_{Ku}^0)} \quad (1)$$

$$P_R = L_Z/N_2 \quad (2)$$

where f is the Ku/C σ^0 relationship (Figure 1a), s is the standard deviation of σ_C^0 (Figure 1b), $N_1 = 2.5$ and $N_2 = 1000$ μm are normalization factors, and L_Z (in microns) is the atmospheric liquid water content expressed as a quadratic polynomial of the three TMR brightness temperatures [*Keihm et al.*, 1995; S. J. Keihm, personal communication, 1995].

In (1) it is assumed that rain probability is proportional to the discrepancy of Ku/C σ^0 and inversely proportional to its standard deviation, while in (2), rain probability is considered to be a linear function of the atmospheric liquid water content and $P_R = 1$ is equivalent to the rain flag used by *AVISO* [1992]. A joint TOPEX/TMR rain probability index is subsequently defined as a linear combination of P_A and P_R,

$$P_J = w_1 P_A + w_2 P_R \quad (3)$$

where $w_1 = 0.75$ and $w_2 = 0.25$ are normalized weights. The choice of w_1 and w_2 is largely based on the geometric ratio of the footprint sizes of the two sensors (42 km for TMR and 5.8 km for TOPEX), assuming that rain probability is uniformly distributed within a TMR footprint and taking into account that a five-point running mean is applied to the altimeter data (i.e., five successive altimeter measurements are used to compute a weighting average within a TMR footprint). In order to fully normalize the three indexes, two cutoff constraints are also applied; that is, probabilities less than 0 or greater than 1 are set to 0 and 1, respectively.

Extensive case studies performed have shown the effectiveness of the rain probability indexes defined above. However, we are not going to describe them in detail, since such descriptions have been well documented in previous studies [*Quartly et al.*, 1996; *Tournadre and Morland*, 1997]. Instead, we will, in the following sections, take advantage of a much longer data duration (1 year compared to 80 days by *Quartly et al.* [1996] and 20 days by *Tournadre and Morland* [1997]) to present some first global and seasonal statistics of the proposed indexes.

3. Rain Frequency: Global/Seasonal Statistics

Obviously, the rain probability indexes proposed in section 2 can also be used as rain flags. In this sense the rain probability at a given measurement location is classified into four categories: (1) certain, $P = 1$; (2) probable, $0.8 \leq P < 1$; (3) possible, $0.5 \leq P < 0.8$; and (4) unlikely, $P < 0.5$.

We first restrict our discussion to rain events which are almost certain and have a look at the relative performances of the three individual indexes. Figure 2 depicts the fraction of cases with $P_{A,R,J} = 1$ (stars, pluses, and circles, respectively), representing the annual variation of global rain frequency suggested by the three indexes. It can be seen that the P_A, P_R, and P_J determined rain frequencies are around 1.2%, 1.0%, and 0.9%, respectively, on the average and the decreasing order remains unchanged throughout the year. Note that 1% is a typical value of rain frequency found in the literature [e.g., *Petty*, 1995]. The TMR rain flag (equivalent to $P_R = 1$) underestimates this parameter, as suggested by *Tournadre and Morland* [1997], while the TOPEX altimeter may slightly overestimate it. The joint index appears to have a compromise value, which agrees with existing knowledge. This agreement supports the choice of weights for P_A and P_R in (3). Figure 2 also shows that the rain frequencies produced by P_A and P_J are slightly lower in the first half of the year than in the second half, but such a variation is not indicated by P_R. Cycles 8 and 24 appear to have much higher rain frequencies according to P_A and consequently P_J, while no corresponding increase is suggested by P_R.

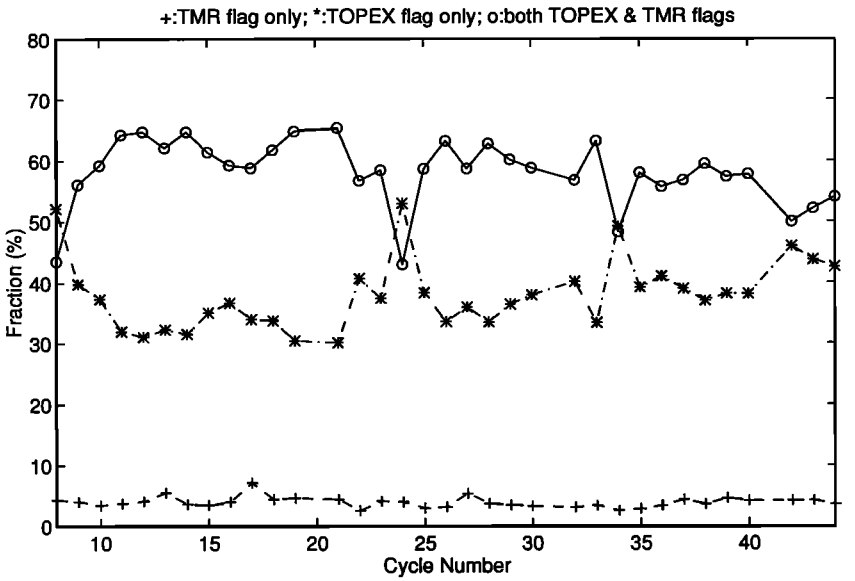

Figure 3. Fraction of measurements for TOPEX cycles 8–44 with $P_J = 1$ and satisfying one of the following conditions: (1) $P_A = 1$ and $P_R = 1$ (circles), (2) $P_A = 1$ and $P_R < 1$ (stars), and (3) $P_A < 1$ and $P_R = 1$ (pluses).

Next, we focus on cases for which $P_J = 1$ and have a look at the consistency between P_A and P_R in triggering P_J. There are three possible combinations of P_A and P_R which can lead to $P_J = 1$: (1) $P_A = 1$ and $P_R = 1$, (2) $P_A = 1$ and $P_R < 1$, and (3) $P_A < 1$ and $P_R = 1$. The fraction of each possibility, denoted by circles, stars, and pluses, respectively, is plotted in Figure 3. This illustrates that about 60% of the cases are simultaneously identified by both P_A and P_R, 36% are triggered by P_A alone, and P_R alone accounts for the remaining 4%. Anomalies associated with cycles 8, 24, and, to some extent, 34 are also present, but cycle 24 is the only one known to have errors in data generation (Table 1).

Furthermore, we may examine the geographical distribution of the 4% cases corresponding to $P_J = 1, P_A < 1$, and $P_R = 1$, i.e., the bottom curve in Figure 3. Although the fraction is small, it appears constantly throughout the year, implying that some geophysical background may exist. We plot these 4% of data as a function of latitude (Figure 4). Surprisingly, the distribution is neither homogeneous nor random; two distinct peaks are found between 40° and 60° in both hemispheres. Note that the two peaks are asymmetric, with the one in the southern hemisphere being higher and narrower. This latitude band falls into the infamous "roaring forties" of maritime lore, a region of high sea state associated with severe weather systems. As a result, wave damping by heavy rain, a topic of active recent research [e.g., *Tsimplis*, 1992; *Atlas*, 1994], is likely to be more significant and frequent than in any other regions, leading to a possible underestimate of rain probability by P_A. In

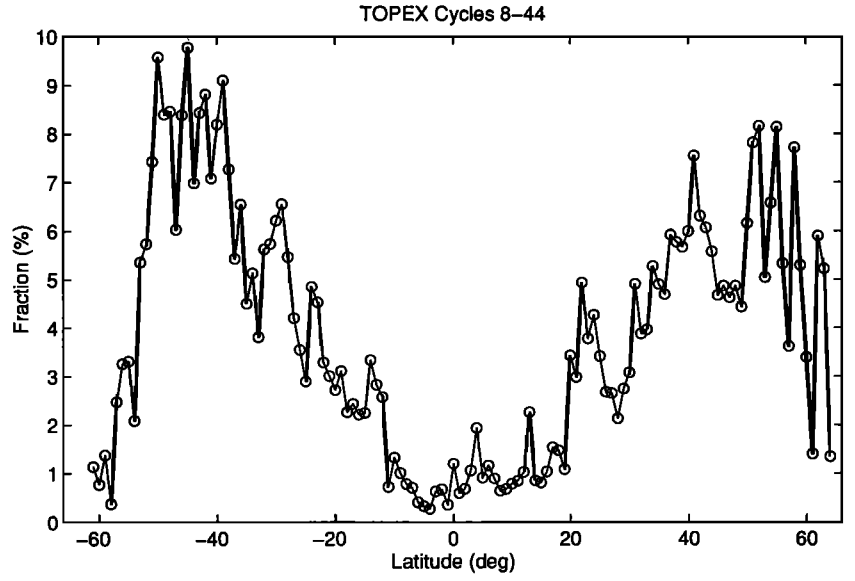

Figure 4. Latitudinal distribution of fraction of measurements satisfying $P_J = 1$, $P_R = 1$, and $P_A < 1$ for TOPEX cycles 8–44.

contrast, P_R should be less affected in this way; a larger contribution to P_J can therefore be expected under such situations.

Keeping in mind the basic statistics discussed above, we now turn our attention to the global/seasonal characteristics of the resulting rain frequency. The geographical locations of the rain events identified by $P_J = 1$ are shown in Figure 5, which consists of four subplots corresponding to cycles 8–16 (December, January, February) (Figure 5a), 17–25 (March, April, May) (Figure 5b), 26–35 (June, July, August) (Figure 5c), and 36–44 (September, October, November) (Figure 5d), respectively. To avoid confusion between rain- and ice-induced σ^0 variations, a sea ice mask derived from ERS 1 scatterometer data [*Gohin and Cavanié*, 1994] is superimposed in grey. Several features in Figure 5 are visible.

1. A zonal band of high rain probability is located along and just north of the equator, coinciding with the Intertropical Convergence Zone (ITCZ), a meteorological feature known as doldrums lying between the trade wind systems of the two hemispheres. The mean location of this band reaches its southernmost position in spring (seasonal names in this paper are referring to the northern hemisphere unless they are otherwise specified) associated with a sharp northern limit (Figure 5b) and northernmost in autumn associated with a sharp southern limit (Figure 5d). Such an annual migration is consistent with that of the ITCZ [*Waliser and Gautier*, 1993].

2. In the southern hemisphere a common feature for the Pacific, Atlantic, and Indian Oceans is that a triangle-shaped "rain-free" zone exists in each of the basins, extending westward from their eastern boundaries. In contrast, three northwest-southeast oriented rain belts can be seen poleward of the dry zones.

3. In the northern hemisphere the geographical pattern of rain frequency has a more remarkable seasonal variation. In the North Pacific away from the ITCZ, a dry-wet-dry zonal structure, corresponding to the trade winds, subtropical highs, and westerlies, can be easily identified. This system undergoes an annual variation with less rain events in winter and spring (Figures 5a and 5b) and more rain events in summer and autumn (Figures 5c and 5d). Moreover, the subtropical rain zone tends to spread in the eastern part of the basin in winter (Figure 5a) and the western part of the basin in summer (Figure 5c), showing an east-west annual oscillation. In the northern Indian Ocean a strong influence of the Asian monsoon on precipitation should be expected. In fact, much more rain activities are observed in the summer and autumn months (Figures 5c and 5d) when the monsoon is active. This is particularly true in the Bay of Bengal and in the Arabian Sea where rain cases are rare during the other half of the year (Figures 5a and 5b). In the North Atlantic the distribution of rain occurrence is largely northeast-southwest oriented, parallel to its boundaries, with higher concentration in the west.

Returning to the beginning of this section, we now examine the behavior of rain frequency for different probability categories. In doing so, we plot the rain frequency as a function of latitude for the three indexes determined by $P_{A,R,J} = 1$, $P_{A,R,J} > 0.8$, and $P_{A,R,J} > 0.5$ (Plates 1a, 1b, and 1c; the TOPEX, TMR, and joint indexes are in blue, green, and red, respectively). It turns out that the general patterns for the certain ($P_{A,R,J} = 1$) and probable ($P_{A,R,J} > 0.8$) rain cases are quite similar (Plates 1a and 1b); those for the possible cases ($P_{A,R,J} > 0.5$) are somewhat different (Plate 1c). The indexes converge in midlatitudes and diverge in tropical and polar regions for all three categories. The decreasing order of P_A, P_J, and P_R in terms of rain frequencies maintained in the diverging bands, while in the converging bands the three indexes are in close competition with a slight lead of P_R. These results confirm the major characteristics exhibited in Figures 2, 3, and 4. Moreover, it is interesting to see that the altimeter flags the rain events twice as much as the radiometer near the equator (Plates 1a–1c). One possible explanation is that the altimeter is more responsive to high freezing levels in the tropics and thus a greater rain column for a given rain rate. Alternatively, this might also be attributable to the possibility that tropical rain occurs more often as intense rain cells which fail to fill the TMR footprint, whereas in midlatitudes, rain occurs more often in large-scale systems with uniform rain rates.

Having examined the relative performances of the three indexes, we extend our comparison to similar results obtained from shipboard present weather reports by *Petty* [1995], which may be the most detailed global climatology to date of the frequency of rain occurrence. In order to be consistent with meteorological classification, we relate $P_J = 1.0$, $0.8 \leq P_J < 1.0$, and $0.5 \leq P_J < 0.8$ to heavy, moderate, and light rain intensity. Thus Plate 1b (including moderate and heavy rains, abbreviated as MH) and Plate 1c (including light, moderate, and heavy rains, abbreviated as LMH) are equivalent to Figure 13 and Figure 12 of *Petty* [1995]. We first compare the MH case, i.e., Plate 1b and Figure 13 of *Petty* [1995]. In the ITCZ between 15°S and 15°N the two results compare quite well; both show a primary peak of about 4% at 7°N and a secondary peak of about 2% at 7°S. Around 20° in both hemispheres, Plate 1b and Figure 13 of *Petty* [1995] show a minimum about 1%. Further poleward up to 60°, both studies show a local maximum in each hemisphere. They agree in that the one in the southern hemisphere appears around 40°S and is weaker than the one in the northern hemisphere. However, the maximum in the northern hemisphere is found at 45°N in Plate 1b, while it is at 60°N in Figure 13 of *Petty* [1995]. Moreover, the peak value of this maximum in Figure 13 of *Petty* [1995] (6%) exceeds the one in the ITCZ and is almost twice that in Plate 1b. Beyond 60°S the rain frequencies produced by the two studies both show a trend of increase, contrary to those implied by previous rain climatologies [e.g., *Jaeger*, 1983; *Legates and Willmott*, 1990]. In fact, this result is one of the important findings in *Petty* [1995] and is independently confirmed by our satellite result. It is necessary to note that the trend of increasing rain frequency in the Southern Ocean results only from the TOPEX index (see the blue curves in Plates 1a–1c). On the contrary, the TMR index (see the green curves in Plates 1a–1c) produces a rapid decrease like most of the SSM/I algorithm in this region [*Petty*, 1997]. This departure serves as an example that the TOPEX and TMR indexes may complement each other. It should be pointed out that the observed feature is unlikely to be due to sea ice contamination, as a result of the effective sea ice mask that we have used. However, the dramatically decreasing number of samples in the COADS data south of 40°S used by *Petty* [1995] may be partly responsible for the discrepancy between the two results (see Plate 2 below).

Next, we turn to the case of LMH, as represented by Plate 1c and Figure 12 of *Petty* [1995]. Features in common include the following. First, the agreement between the two results in the ITCZ is as good as the previous case, both showing a pair of peaks around 10% and 5%, respectively. Second, the two midlatitude maxima become less well-defined compared to the previous case, particularly the one in the southern hemisphere.

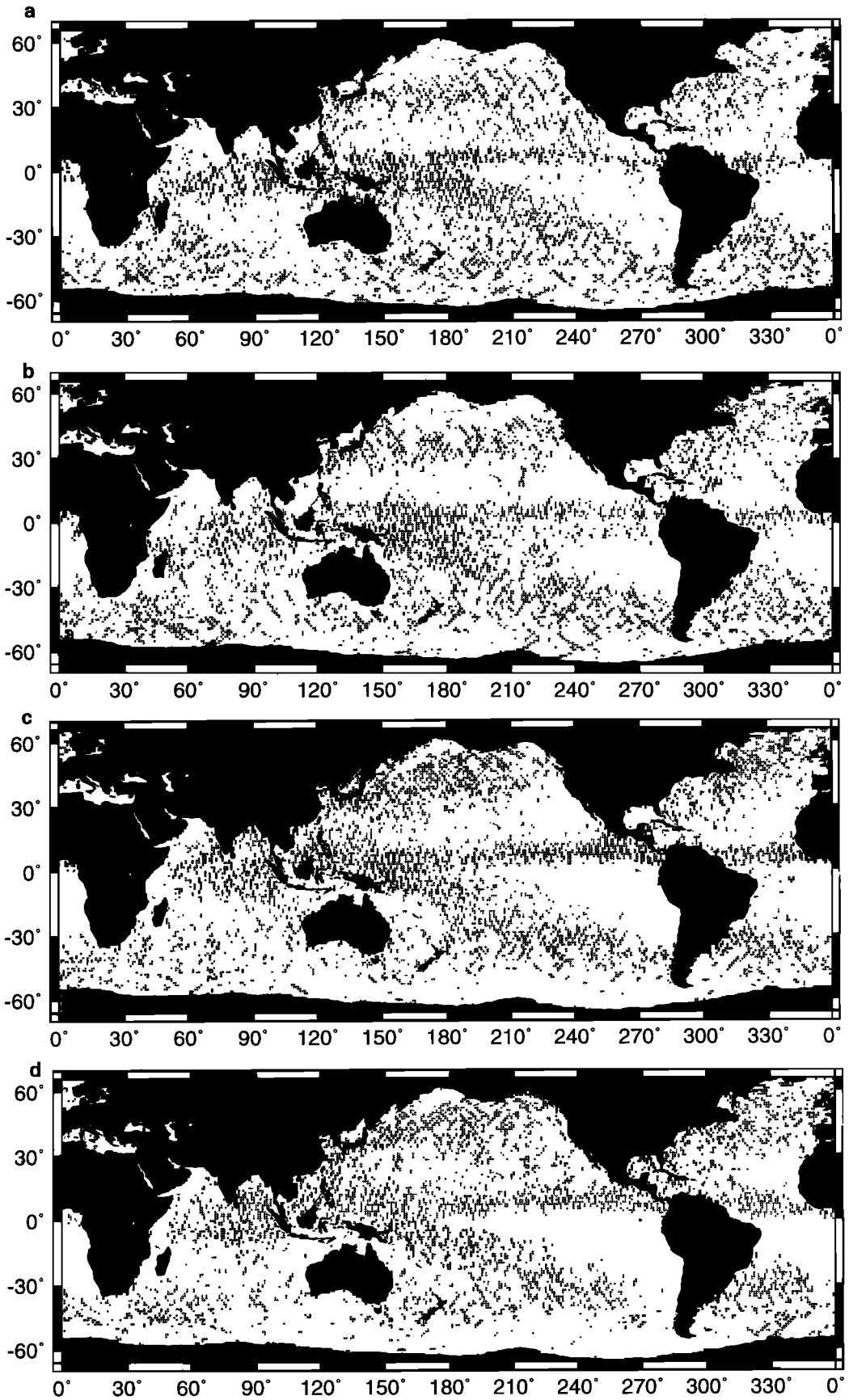

Figure 5. Locations of certain rain cases identified by the joint TOPEX/TMR rain probability index (P_J = 1) for (a) cycles 8–16, (b) cycles 17–25, (c) cycles 26–35, and (d) cycles 36–44. Areas in grey are sea ice masks derived from ERS 1 scatterometer data.

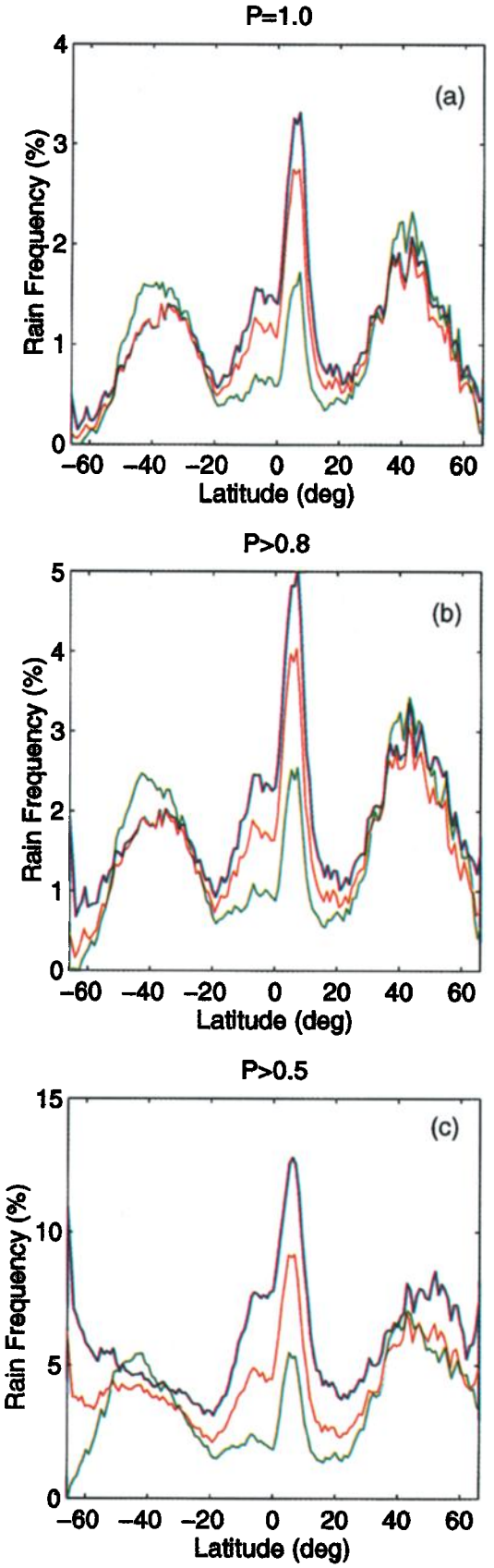

Plate 1. Zonally averaged rain frequency for TOPEX cycles 8–44 determined by P_A (in blue), P_R (in green), and P_J (in red) corresponding to (a) certain ($P_{A,R,J} = 1$), (b) probable ($P_{A,R,J} \geq 0.8$), and (c) possible ($P_{A,R,J} \geq 0.5$) rain events.

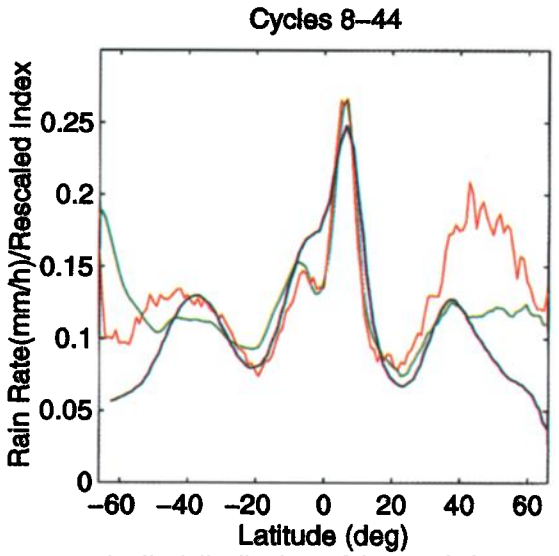

Plate 2. Latitudinal distributions of the rescaled average rain probability index ($\bar{P}_{i,j}$) for TOPEX cycles 8–44 (in red), the GPCP precipitation rate (in millimeters per hour) determined by using multisatellite data between December 1992 and November 1993 (in blue), and the mean rain rate (in millimeters per hour) derived from COADS data collected during 1945–1989 (in green).

Third, both results show a poleward increase of rain frequency in the Southern Ocean, as already been noted in the previous case. However, considerable differences lie in that ship-observed rain frequency is systematically higher than satellite identification by a factor of 2 outside the ITCZ. Several reasons may be responsible for any differences in the comparison. Uncertainties associated with ship observations may come from extremely inhomogeneous sampling in space and time, systematic misclassification by inexperienced observers, "fair" or "foul" weather bias, mislocation, etc. (see *Petty* [1995] for a detailed discussion). On the other hand, satellite measurements are subjected to various atmospheric and meteorological perturbations, sensor noises (magnified by using multifrequency data), footprint mismatch between TOPEX and TMR, and so on. In addition, one must not forget that the COADS data used by *Petty* [1995] were collected between 1958 and 1991, not covering the period of the TOPEX/TMR data used in this study (see Table 1).

In summary, ship-observed and TOPEX/TMR-identified MH and LMH rain frequencies show quantitative agreement in the ITCZ, while they show qualitative agreement in other regions. Taking into account the fact that the comparisons are made without any altimeter rain calibration/validation, the performance and potential of TOPEX rain detection are remarkable.

4. Rain Probability: Global/Seasonal Characteristics

In this section we go one step further in our analysis by employing an averaged rain probability index, finding its correlation with independent precipitation climatologies, and examining its regional/seasonal variations.

The individual rain probabilities defined by (3) are binned into 1° × 1° boxes, and an averaged rain index for each box, $\bar{P}_{i,j}$, is introduced as

$$\bar{P}_{i,j} = \frac{\sum_{m=1}^{M_{i,j}} (P_j)_{i,j,m}}{M_{i,j} + N_{i,j}} \qquad (P_j)_{i,j,m} \geq 0.5 \qquad (4)$$

$$i = 1, 2, \cdots, 360 \qquad j = -66, -65, \cdots, 65, 66$$

where i and j are longitude and latitude in degrees and $M_{i,j}$ and $N_{i,j}$ are the number of points with their individual rain probabilities over or under 0.5 within each grid box. Note that the inclusion of $N_{i,j}$ is necessary in order to avoid the "foul weather bias."

4.1. Zonal Variation

The zonally averaged rain probability index is rescaled and plotted in Plate 2 (the red curve), along with the GPCP multisatellite precipitation rate (the blue curve), as well as the precipitation climatology obtained from COADS (the green curve). The rescaling factor is determined by a least squares fit of the TOPEX/TMR rain index to the GPCP rain rate within 30°S–30°N. The GPCP data used here are a weighted combination of SSM/I, GOES, GMS, and Meteosat rain rate estimates [*Huffman et al.*, 1997] with a spatial resolution of 2.5° × 2.5° longitude/latitude and a temporal coverage from December 1992 to November 1993 (corresponding to TOPEX cycles 8–44), while the COADS rain rate is a 1° × 1° global climatology derived from a massive number of individual ship reports collected between January 1945 and December 1989 using objective analysis [*da Silva et al.*, 1994]. By and large the averaged TOPEX/TMR index is able to produce most of the latitudinal oscillations of rain rate suggested by GPCP and COADS, although some of the corresponding peaks and troughs are shifted, as seen in Plate 2. Fairly good agreement is found in the tropical and subtropical oceans, especially between the TOPEX and COADS estimates. The secondary peak of the southern ITCZ is less well defined in the GPCP compared to the other two data sets, probably because of its coarser spatial resolution (2.5° versus 1°). And perhaps for the same reason, the primary peak of GPCP in the ITCZ is also lower than the others. In midlatitude areas the TOPEX/TMR and GPCP results both display a maximum in each hemisphere, although their locations and intensities are different. This feature, however, is much less significant in the COADS result. The systematically higher precipitation around 50°N suggested by the TOPEX/TMR is worth noting. It is unlikely that this can be attributed to the differences in spatial resolution or temporal coverage of various data sources. But at this stage we do not have a satisfactory explanation. The largest discrepancy of the three rain estimates seems to be in the subpolar regions (Plate 2). Interestingly, however, the TOPEX/TMR and COADS curves converge steadily toward 65°S and 65°N. The poleward increase of rainfall toward the Antarctic reappears in both TOPEX/TMR and COADS results. On the contrary, the GPCP result shows a decreasing trend toward both poles, implying that the present multisatellite precipitation algorithms may considerably underestimate the rain intensity over subpolar regions. Nevertheless, in view of the agreement and difference of the above comparisons, it is quite clear that useful and complementary information of oceanic rain rate can be extracted from the proposed TOPEX/TMR rain index.

4.2. Global Distribution

The simultaneous global distributions of the TOPEX/TMR rain index, $\bar{P}_{i,j}$, and the GPCP precipitation rate are shown in Plates 3a and 3b, respectively, both of which are annual averages within the same period of December 1992 and November 1993. In addition, the COADS rainfall climatology for the period between 1945 and 1989 [*da Silva et al.*, 1994] is also included for comparison (Plate 3c). At first sight it is already evident that the general agreement is surprising, except for most of the features in the GPCP map (Plate 3b) being smoother as a result of its lower spatial resolution. A closer inspection allows at least the following characteristics to be identified.

1. The three distributions are all dominated by a zonally banded structure which has to be understood in relation with atmospheric circulation. Moving eastward along the equator, a prominent rain belt crossing the Pacific, the Atlantic, and the Indian Oceans can be found. This belt, associated with persistent cloudiness, results from the trade winds which blow from approximately the east-northeast in the northern hemisphere and the east-southeast in the southern hemisphere and converge just north of the equator in the ITCZ. Because of the asymmetrical distribution of land masses and attendant heat storage between the hemispheres, the ITCZ is actually located at an average of 7° north of the equator and is effectively the thermal and meteorological equator. There is not much difference in the mean location of this rain belt in Plates 3a, 3b, and 3c. However, the extent and area of maximum intensity appear to be less consistent. In the tropical Pacific Ocean a very strong rain belt is observed between 180° and 220°E in the COADS map (Plate 3c), in contrast to the relatively low rainfall intensity there in the TOPEX/TMR and GPCP maps (Plates 3a and 3b). In the topical Indian Ocean the GPCP suggests a less intensive and less concentrated rain zone off west Indonesia compared to the TOPEX/TMR and COADS results.

2. Within the latitude band between 10° and 30°S, three northwest-southeast oriented dry zones exist in each of the basins. Their northern hemisphere counterparts can be found within the same latitude band. The six dry zones are hereinafter referred to as "marine deserts," since they are equivalent to the continental deserts which prevail at these latitudes. The six marine deserts are well defined in Plates 3a, 3b, and 3c. A common feature shared by the TOPEX/TMR and GPCP maps is that the three deserts in the southern hemisphere are much drier than their northern hemisphere counterparts. But this is not obvious for the COADS climatology, probably owing to the different period and duration. It is not difficult to explain the existence of these marine deserts. The rising air leaving the rotating surface near the equator must conserve its absolute angular momentum and move poleward. At high altitudes it radiatively cools by emitting long wave infrared radiation and thereby becomes denser. By the time the poleward flowing air has reached 25°–30° latitude, it has acquired an appreciable easterly or zonal component, has dried considerably through rainfall, and begins to sink, forming a desert region globally.

3. Poleward from 20°S, one can find three parallel rain belts, respectively extending southeastward from eastern Indonesia to the South Pacific (corresponding to the South Pacific convergence zone (SPCZ)), from Uruguay to the South Atlantic (corresponding to the South Atlantic Convergence Zone (SACZ)), and from Madagascar to the South Indian Ocean, respectively. Next to these rain belts, a dry belt related to the subtropical highs with its mean position varying from 40° to 55°S is visible. Farther south, an increasing trend toward the Antarctic is seen in Plates 3a and 3c, while a decreasing trend appears in Plate 3b. In the northern hemisphere, poleward from 20°N, two rain belts resulting from midlatitude westerlies

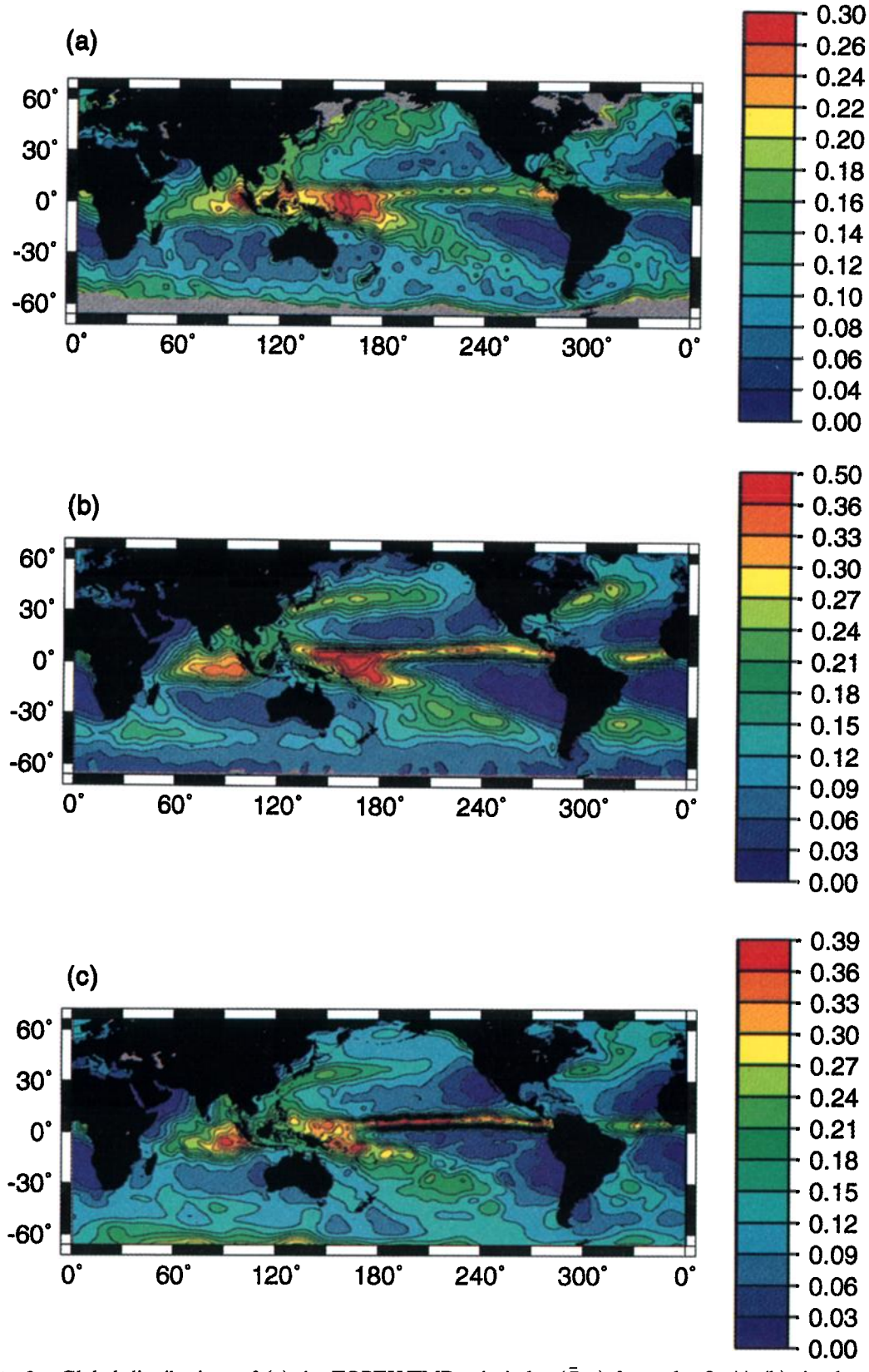

Plate 3. Global distributions of (a) the TOPEX/TMR rain index ($\bar{P}_{i,j}$) for cycles 8–44, (b) simultaneous GPCP precipitation rate (in millimeters per hour) derived from multisatellite data collected between December 1992 and November 1993, and (c) the COADS rainfall climatology (in millimeters per hour) for the period between 1945 and 1989. Areas in grey are sea ice masks derived from ERS 1 scatterometer data.

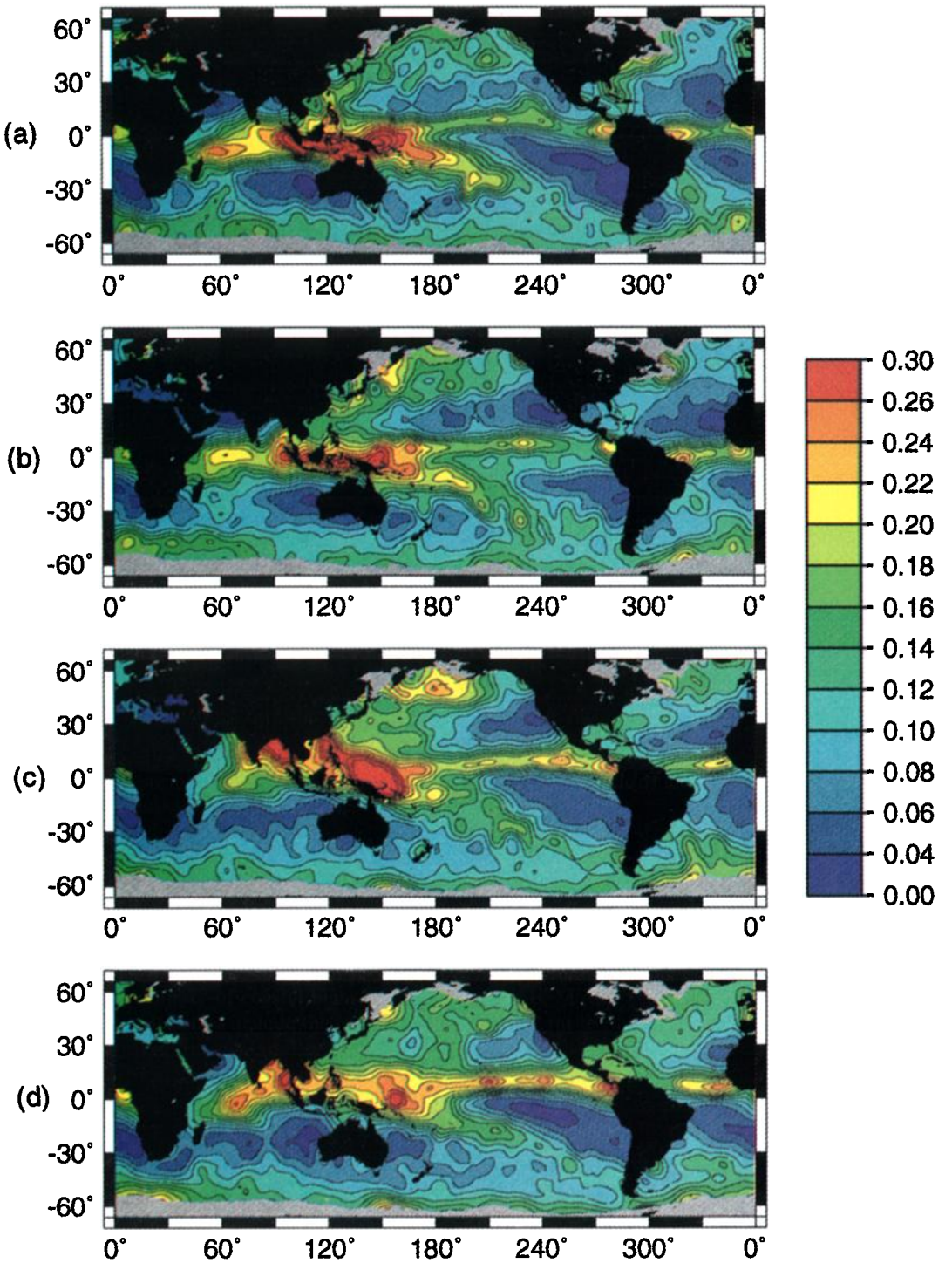

Plate 4. Seasonal variations of the TOPEX/TMR rain index ($\bar{P}_{i,j}$) for northern hemisphere (a) winter (cycles 8–16), (b) spring (cycles 17–25), (c) summer (cycles 26–35), and (d) autumn (cycles 36–44). Areas in grey are sea ice masks derived from ERS 1 scatterometer data.

are identifiable in the North Pacific and North Atlantic. They are well defined in Plates 3b and 3c but poorly defined in Plate 3a. North of 45°N, the three results again differ remarkably: Plate 3a suggests a steady increase in rain intensity, while Plates 3b and 3c show a slow decrease.

4. It is worth noting a number of coastal highs which appear in Plate 3a. The areas identified include the Mozambique Channel, the East China Sea, the surrounding waters of Sakhalin Island, Tasmania, New Zealand and the United Kingdom, the east coast of Canada, the Florida Peninsula, the Gulf of Guinea, and the east coast of Uruguay. On the other hand, several regional lows can also be recognized in some semi-enclosed seas such as the Arabian Sea, the Bay of Bengal, the South China Sea, the Sea of Japan, the Hudson Bay, and the Gulf of Mexico (Plate 3a). These local features are often less significant in Plate 3b as a result of its coarser grid. However, some of the differences in local rain intensities between the two maps are too large to be explained by this reason. For example,

the western coastal wet zones off northeast America and northeast Asia seen in Plate 3a are much drier in Plate 3b. In fact, similar divergence for these regions can be found in published precipitation maps [e.g., *Baumgartner and Reichel*, 1975; *Reed and Elliott*, 1979; *Dorman and Bourke*, 1981]. Some of the authors argue that the differences could be attributed to measured rainfall associated with local land thunderstorm rainfall not representative of the marine area [*Dorman and Bourke*, 1981]. In contrast to this argument, there is increasing evidence that oceanic precipitation variations are linked to changes in regional weather and climate over the continents [e.g., *Trenberth and Branstator*, 1992]. In light of the result obtained here (Plate 3a), we feel that the reasons for such systematic regional differences need to be reinvestigated. It was suspected, at the beginning, that some of the local highs may be induced by small island contamination on radar backscatter. A careful land/water screening is performed to remove measurements obtained in waters shallower than 50 m using a high-resolution (5′ × 5′) global relief data (ETOPO5) released by the National Oceanic and Atmospheric Administration/National Geophysical Data Center. This seems to have little impact on most of the observed anomalies. Therefore such a possibility could almost be ruled out.

By now, there is little doubt that valuable rain information has been extracted from the TOPEX altimeter and the TMR radiometer. We believe that Plate 3a offers a new look at the spatial distribution of global precipitation and serves as an instructive basis for further investigation of relevant regional and seasonal features.

4.3. Seasonal Change

To examine the seasonal change in global oceanic precipitation, cycles 8–44 of the TOPEX data are divided into the same four subsets as for Figure 5. Strictly speaking, the word "seasonal" is not very accurate in this circumstance, since the data used in our analysis are only of 1-year duration which do not allow us to follow interannual variations. We nevertheless use this term in our discussion for simplicity while keeping its drawback in mind. Certainly, the prospect of being able to follow interannual variations in the behavior of the ITCZ, SPCZ, etc., is very exciting, as many other data sets are either low resolution (e.g., GPCP) or produced through averaging of many years data (e.g., COADS). The $\bar{P}_{i,j}$ distributions corresponding to the four seasons are shown in Plate 4. Several impressive features are described below.

1. The rainfall distribution is dominated by large-scale tropical features throughout the year. These features include the maxima along the ITCZ, the SPCZ, the SACZ, and the Indonesian area of the eastern Indian Ocean. The tropical rainfalls in these regions undergo an annual process of north-south seesaw. For example, the Pacific ITCZ reaches its southern extreme in spring, while northern extreme is in autumn (Plates 4b and 4d), as also observed with rain frequency (Figures 5b and 5d). This is somehow different from the result by *Legates and Willmott* [1990] that very heavy rain occurs just north of the equator in July and August and south of the equator in January and February. One of the most significant seasonal rainfall variations in the midlatitudes of both hemispheres is known to be associated with storm tracks. For instance, the extratropical storm tracks extending eastward and poleward from southern Japan, the northeast United States, and southeast Brazil are quite evident in the MSU-derived global oceanic precipitation map during March, April, and May [*Spencer*, 1993]. However, such features are not very well displayed in our seasonal maps (Plates 4a–4d), possibly as a result of the sampling scheme of satellite altimetry. Another characteristic which can be seen in Plate 4 is that precipitation variability is considerably damped over the extensive Southern Ocean due to the moderating effects of the oceans on precipitation.

2. An east-west annual migration of an enhanced rain zone within the ITCZ is observed in all three basins. In the northern hemisphere winter, rainfall intensification starts from eastern Indonesia in the Pacific, from the north coast of Brazil in the Atlantic, and from northeast of Madagascar in the Indian Ocean (Plate 4a). During the spring months, three intensified equatorial rain zones, one in each basin separated from their western origins, are on the way to the east coasts (Plate 4b). When summer comes, they seem to have arrived in their eastern destinations: central America in the Pacific, the west coast of Guinea in the Atlantic, and the western island of Indonesia in the Indian Ocean, forming a significant enhancement of rainfall around those areas (Plate 4c). In autumn a return journey is seen as a series of local maxima in the central Pacific, a single maximum in the central Atlantic, and a westward meandering in the central Indian Ocean, accompanied by a rapid weakening of rain intensity around both the east and west boundaries of the basins (Plate 4d). It is important to recognize that there is a coherent pattern of association of regional rainfall with ENSO. For example, there is growing evidence that fluctuations in the African monsoon circulations and associated rainfall are predictable [*World Climate Research Program* (*WCRP*), 1995]. The domain of summer rainfall extending from the West African Sahel into Ethiopia and the western part of the east African highland has a positive correlation with ENSO. Understanding rainfall and its variability will contribute significantly to making reliable ENSO and monsoon forecasts.

3. Going through the seasonal precipitation maps (Plates 4a–4d), a general phase opposition between the two hemispheres is discernible. The phase relationship can be better revealed by plotting the rain index with respect to cycle number for each hemisphere (Figure 6). It can be seen that on global scale excluding the polar and subpolar regions, precipitation of each hemisphere is peaked in its warmer months of the year, resulting in a general phase reversal between the two hemispheres. On top of that, seasonal oscillations are also apparent for both hemispheres. The northern hemisphere (circles in Figure 6) appears to have a primary peak in October (cycle 39) and a flat peak around June (cycles 26–34), while the southern hemisphere (pluses) appears to have a broad high from late December to early May (cycles 8–23). The global mean (stars), however, seems to have little seasonality. It is also clear from Figure 6 that the average rain intensity of the northern hemisphere is higher than that of the southern hemisphere during the whole year, with the difference being the greatest in early autumn. Furthermore, the magnitude of seasonal precipitation variation is larger in the northern hemisphere than in the southern hemisphere by nearly a factor of 2. This is partly the result of the larger oceanic areas in the southern hemisphere which moderate seasonal changes.

4. It is interesting to have a closer look at the seasonal evolution of the six marine deserts. Systematic migration occurs for the North Pacific desert, whose westernmost position is found in the central western Pacific during wintertime (Plate 4a), while its easternmost position is found along the west coast of the United States in summer (Plate 4c). The South Pacific

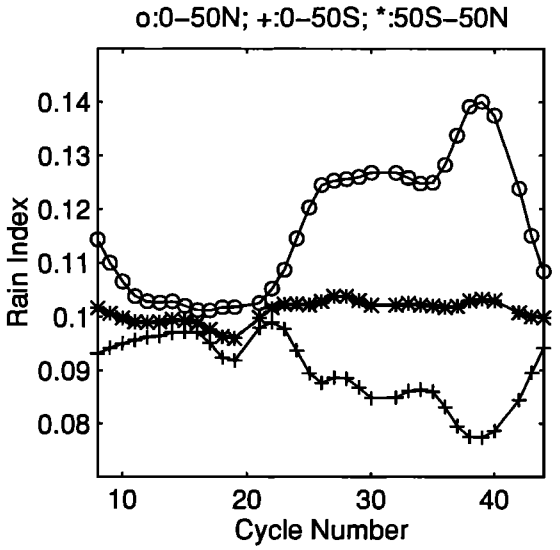

Figure 6. Temporal variations of the TOPEX/TMR rain index ($\bar{P}_{t,j}$) averaged over 0–50°N (circles), 0–50°S (pluses), and 50°S–50°N (stars) for cycles 8–44.

desert undergoes an annual cycle of expansion and contraction, increasing to a maximum size in autumn (Plate 4d) and shrinking to a minimum size in spring (Plate 4b). The North Atlantic and South Indian Ocean deserts are characterized by a process of merging and breakup: The former merges in summer and breaks in other seasons, while the latter merges in winter and breaks during the rest of the year. The South Atlantic desert has little change in position and pattern throughout the year, except a weaker intensity in spring (Plate 4b). The North Indian Ocean desert is somewhat different from others due to its special geographical location and climatic condition. It is the smallest one among the six deserts, oscillating slightly with seasons along the coast of the Arabian Sea.

5. A number of local precipitation anomalies along the world coasts have been noted in Plate 3a. Following these features in the seasonal maps (Plates 4a–4d), one finds that most of them are time dependent rather than persistent. For instance, intensified rainfall in the Mozambique Channel is only seen in winter (Plate 4a). The enhanced maxima related to the western Pacific storm track start to form in the East China Sea during spring and extend to the surrounding waters of Japan in summer (Plates 4b and 4c). They almost vanish during the other half of the year (Plates 4a and 4d) and consequently become less visible in the annual map (Plate 3a) as a result of seasonal averaging. The rainfall around Florida peaks in autumn, leading to a subsequent narrowing of the dry zone in the Gulf of Mexico (Plate 4d). The local minimum in the Bay of Bengal is nudged off the coast in summer when the Indian monsoon and its associated heavy precipitation prevail (Plate 4c). As a result the summer rainfall pattern in this area is characterized by the coexistence of a prominent maximum in the northeast and a weakened minimum in the southwest.

From the preliminary analysis presented above, it is evident that 1 year's TOPEX and TMR data have allowed us to capture and delineate the major seasonal characteristics of global oceanic precipitation. It is hopeful that the expected 5-year TOPEX/TMR data will enable us to confirm these results, particularly those previously unknown features, and eventually to investigate the interannual variability of rainfall and its relation with ENSO which has a 2- to 4-year cycle and a strong dependence as well as influence on global and regional climate.

5. Summary and Final Remarks

The work presented here is primarily a feasibility study on the observation of global oceanic precipitation by TOPEX and TMR. The results obtained have clearly demonstrated the effectiveness and potential of the proposed methodology. Key contributions to its success include the following. First, the introduction of a rain probability index, which is an outgrowth of various thresholds used earlier, has enabled us to quantify rain effects on altimeter and radiometer measurements and relate them to rain frequency and intensity. The second contribution is the unique role of TOPEX, which results from the fact that TOPEX is the first dual-frequency altimeter and is perhaps also the first active spaceborne sensor used to derive precipitation maps over the ocean. An important advantage of an active microwave system is that it allows the two-way attenuation to be measured, leading to an improved efficiency in rain detection compared to a passive system. Third, the joint use of TOPEX and TMR has shown that the complementarity of the two sensors in rain detection is largely latitude dependent. In the tropics the two measurements usually differ by a factor of 2. In midlatitude areas the TOPEX altimeter tends to underestimate the rainfall due to possible wave damping, while the TMR is hardly affected by this effect. In subpolar regions where the radiometer is almost ineffective, the altimeter is seen to have a better performance. Despite the above-mentioned strengths the weaknesses of the present methodology should also be pointed out. For instance, the proposed rain probability index cannot, at this stage, provide a direct and quantitative estimate of rain rate. An attempt to establish an empirical relation between them is currently underway. In addition, the TOPEX altimeter can only detect rain events at nadir points along fixed ground tracks. This is obviously a disadvantage compared to the wide swath radiometer like SSM/I.

This work is also a step toward constructing a TOPEX/TMR precipitation climatology. Attempts have been made to compare our results with those from the GPCP and COADS rain climatologies. In terms of rain frequency, TOPEX/TMR and COADS show quantitative agreement in the ITCZ and qualitative agreement in other regions. Recalling that more than two thirds of the global precipitation falls in the tropics and subtropics, such an agreement is encouraging. On the basis of a rain index combining TOPEX and TMR, annual and seasonal precipitation maps are constructed which, to our knowledge, are the first of their kind. On global scale the three basins bear a number of similarities such as a prominent rain belt in the ITCZ, a dry zone in the subtropics of each hemisphere, and a northwest-southeast oriented rain belt in the southwestern part of each basin (Plate 3a). Comparisons with simultaneous GPCP multisatellite precipitation rate and COADS rain climatology suggest that systematic differences also exist. One example is that the maximum rainfall in the ITCZ of the Indian Ocean appears to be more intensive and much concentrated in our result (Plate 3a) compared to that of the GPCP (Plate 3b). Another example is that the annual precipitation produced by TOPEX/TMR is constantly higher than those from GPCP and COADS in most of the extratropical regions of the northern hemisphere, especially along the northwest coasts of the Pacific and Atlantic Oceans (Plates 2 and 3). On regional scale, notable features are several local maxima and minima of rain

intensity along the world coasts or around some islands. The identified areas include the Mozambique Channel, the Arabian Sea, the Bay of Bengal, the East and South China Seas, the Sakhalin, Tasmania, and New Zealand islands, the east coasts of Uruguay and Canada, the Hudson Bay, the Florida Peninsula, and the Gulf of Mexico (Plates 3a and 4). Seasonality is a common feature on both global and regional scales. A general phase reversal of oceanic rainfall is discernible between the two hemispheres. An east-west annual migration of an enhanced rain zone within the ITCZ is observed in all three basins. The seasonal evolution of the six marine deserts follows several patterns such as systematic migration (the North Pacific and North Indian Oceans), expansion and contraction (the South Pacific Ocean), merging and breakup (the North Atlantic and South Indian Oceans), and pure intensity variation (the South Atlantic Ocean). The seasonality of regional features is largely influenced by local atmospheric events such as the monsoon, storm, or snow activities.

Finally, we would like to stress that the first satellite mission dedicated to rain measurement, the Tropical Rainfall Measuring Mission scheduled to be launched in 1997, will only be carrying a single-frequency rain radar operating at 13.8 GHz plus three multifrequency radiometers [*Simpson et al.*, 1988]. Therefore TOPEX and its follow-on will remain as the only dual-frequency radar in orbit for some years to come. They will serve as an important component in observing global oceanic precipitation with the advantages of being simple, complementary, and "costless."

Acknowledgment. This work has benefited from a grant by the French Foreign Affair Ministry in support of Ge Chen's stay at IFREMER.

References

Archiving, Validation, and Interpretation of Satellite Data in Oceanography (AVISO), AVISO user handbook: Merged TOPEX/POSEIDON products, *AVI-NT-02-101-CN*, ed. 2.1, 213 pp., Cent. Natl. d'Etudes Spatiales, Toulouse, France, 1992.

Atlas, D., Footprints of storms on the sea: A view from spaceborne synthetic aperture radar, *J. Geophys. Res.*, *99*, 7961–7969, 1994.

Barrett, E. C., and D. W. Martin, *The Use of Satellite Data in Rainfall Monitoring*, 340 pp., Academic, San Diego, Calif., 1981.

Baumgartner, A., and E. Reichel, *The World Water Balance*, 179 pp., Elsevier, New York, 1975.

Black, P. G., R. C. Gentry, V. J. Cardone, and J. D. Hawkins, Seasat microwave wind and rain observations in severe tropical and midlatitude marine storms, *Adv. Geophys.*, *27*, 198–278, 1985.

Cheng, M., and R. Brown, Delineation of precipitation area by correlation of Meteosat visible and infrared data with radar data, *Mon. Weather Rev.*, *123*, 2743–2757, 1995.

da Silva, A. M., C. C. Young, and S. Levitus, *Atlas of Surface Marine Data 1994*, vol. 1, *Algorithms and Procedures*, *NOAA Atlas NESDIS 6*, 83 pp., Natl. Oceanic and Atmos. Admin., Washington, D. C., 1994.

Dorman, C. E., and R. H. Bourke, Precipitation over the Atlantic Ocean, 30°S to 70°N, *Mon. Weather Rev.*, *109*, 554–563, 1981.

Gohin, F., and A. Cavanié, A first try at identification of sea ice using the three beam scatterometer of ERS-1, *Int. J. Remote Sens.*, *15*, 1221–1228, 1994.

Goldhirsh, J., and E. Walsh, Rain measurements from space using a Seasat type altimeter, *IEEE Trans. Antennas Propag.*, *30*, 726–733, 1982.

Guymer, T. H., G. D. Quartly, and M. A. Srokosz, The effects of rain on ERS-1 radar altimeter data, *J. Atmos. Oceanic Technol.*, *12*, 1229–1247, 1995.

Huffman, G. J., R. F. Adler, P. A. Arkin, A. Chang, R. Ferraro, A. Gruber, J. Janowiak, A. McNab, B. Rudolf, and U. Schneider, The Global Precipitation Climatology Project (GPCP) combined precipitation data set, *Bull. Am. Meteorol. Soc.*, *78*, 5–20, 1997.

Jaeger, L., Monthly and areal patterns of mean global precipitation, in *Variations in the Global Water Budget*, edited by A. Street-Perrott, M. Beran, and R. Ratcliffe, pp. 129–140, D. Reidel, Norwell, Mass., 1983.

Janowiak, J. E., and P. A. Arkin, Rainfall variations in the tropics during 1986–89, as estimated from observations of cloud-top temperature, *J. Geophys. Res.*, *96*, 3359–3373, 1991.

Jet Propulsion Laboratory, California Institute of Technology, *Seasat Gulf of Alaska Workshop Report*, vol. 1, *NASA Panel Rep.*, *G22-101*, 1979.

Keihm, S. J., M. A. Janssen, and C. Ruf, TOPEX/Poseidon microwave radiometer (TMR), III, Wet troposphere range correction algorithm and prelaunch error budget, *IEEE Trans. Geosci. Remote Sens.*, *33*, 147–161, 1995.

Legates, D. R., and C. J. Willmott, Mean seasonal and spatial variability in gauge corrected, global precipitation, *Int. J. Climatol.*, *10*, 111–127, 1990.

Olsen, R. L., D. V. Rogers, and D. B. Hodge, The aR^b relation in the calculation of rain attenuation, *IEEE Trans. Antennas Propag.*, *AP-26*, 318–329, 1978.

Petty, G. W., Frequencies and characteristics of global oceanic precipitation from shipboard present-weather reports, *Bull. Am. Meteorol. Soc.*, *76*, 1593–1616, 1995.

Petty, G. W., An intercomparison of oceanic precipitation frequencies from 10 special sensor microwave/imager rain rate algorithms and shipboard present weather reports, *J. Geophys. Res.*, *102*, 1757–1777, 1997.

Petty, G. W., and K. B. Katsaros, Nimbus-7 SMMR precipitation observations calibrated against surface radar during TAMEX, *J. Appl. Meteorol.*, *6*, 489–505, 1992.

Quartly, G. D., T. H. Guymer, and M. A. Srokosz, The effects of rain on TOPEX radar altimeter data, *J. Atmos. Oceanic Technol.*, *13*, 1207–1227, 1996.

Reed, R. K., and W. P. Elliott, New precipitation maps for the North Atlantic and North Pacific Oceans, *J. Geophys. Res.*, *84*, 7839–7846, 1979.

Simpson, J., R. F. Adler, and G. R. North, A proposed Tropical Rainfall Measuring Mission (TRMM) satellite, *Bull. Am. Meteorol. Soc.*, *69*, 278–295, 1988.

Spencer, R. W., Global oceanic precipitation from the MSU during 1979–1991 and comparisons to other climatologies, *J. Clim.*, *6*, 1301–1326, 1993.

Srokosz, M. A., and T. H. Guymer, A study of the effect of rain on Seasat radar altimeter data, in *Proc. IGARSS'88 Symp.*, *Eur. Space Agency Spec. Publ.*, *ESA SP-284*, 651–654, 1988.

Tournadre, J., and J. C. Morland, The effects of rain on TOPEX/POSEIDON altimeter data: A new rain flag based on Ku and C band backscatter coefficients, *IEEE Trans Geosci. Remote Sens.*, in press, 1997.

Trenberth, K. E., and G. W. Branstator, Issues in establishing causes of the 1988 drought over North America, *J. Clim.*, *5*, 159–172, 1992.

Tsimplis, M., The effect of rain in calming the sea, *J. Phys. Oceanogr.*, *22*, 404–412, 1992.

Waliser, D. E., and C. Gautier, A satellite derived climatology of the ITCZ, *J. Clim.*, *6*, 2162–2174, 1993.

Wilheit, T., et al., Algorithms for the retrieval of rainfall from passive microwave measurements, *Remote Sens. Rev.*, *11*, 163–194, 1994.

Woodruff, S. D., R. J. Slutz, R. L. Jenne, and P. M. Steuer, A comprehensive ocean-atmospheric data set, *Bull. Am. Meteorol. Soc.*, *68*, 1239–1250, 1987.

World Climate Research Program, Science plan for the World Climate Research Program, *WCRP Publ. 89*, *WMO/TD-690*, World Meteorol. Organ., Geneva, Switzerland, 1995.

B. Chapron, K. Katsaros, and J. Tournadre, Département d'Océanographie Spatiale, Centre de Brest, IFREMER, BP 70, 29280 Plouzané, France.

G. Chen, Ocean Remote Sensing Institute, Ocean University of Qingdao, 5 Yushan Road, Qingdao 266003, China. (e-mail: mxhe@ns.qd.sd.cn)

D. Vandemark, Laboratory for Hydrospheric Processes, Wallops Flight Facility, NASA Goddard Space Flight Center, Code 972, Building 159, Wallops Island, VA 23337.

(Received June 25, 1996; revised December 6, 1996;
accepted December 30, 1996.)